water
MDPI

Article

Characterizing Density Flow Regimes of Three Rivers with Different Physicochemical Properties in a Run-Of-The-River Reservoir

Ingu Ryu [1], Soonju Yu [1] and Sewoong Chung [2,*]

[1] Han River Environment Research Center, National Institute of Environmental Research (NIER), 42, Dumulmeori-gil 68 beon-gil, Yangseo-myeon, Yangpyeong-gun, Gyeonggi-do 12585, Korea; ilovmi@korea.kr (I.R.); ysu1221@korea.kr (S.Y.)

[2] Department of Environmental Engineering, Chungbuk National University, Chungdae-ro 1, Seowon-gu, Cheongju-si, Chungcheongbuk-do 28644, Korea

* Correspondence: schung@chungbuk.ac.kr; Tel.: +82-43-261-3370

Received: 8 February 2020; Accepted: 3 March 2020; Published: 6 March 2020

Abstract: Inflow mixing affects the spatiotemporal heterogeneity of water quality in reservoirs. Reservoir water quality management requires accurate prediction of density flow regimes to understand the spatiotemporal distribution of dissolved and particulate nutrients and organics. This study aims to characterize the mixing and circulation of three rivers with different physicochemical properties in a run-of-the-river (ROR) reservoir, using high-frequency monitoring and three-dimensional (3D) hydrodynamic modeling. The Aquatic Ecosystem Model (AEM3D) was constructed for the reservoir and calibrated with high-frequency data obtained from May–June 2016, accurately reproducing the observed spatiotemporal variations of flow velocity, water temperature, and electrical conductivity (EC) in the reservoir. High-frequency data and 3D model results showed that mixing of the rivers in the ROR reservoir is governed by density flow regimes formed by influent water temperature differences. At the confluence, colder and warmer river influents formed underflows and surface buoyant overflows, respectively. The spatial arrangement of flow direction, water residence time, and EC concentration were largely controlled by the buoyancy-driven flow. Stagnant areas with long residence times corresponded with areas of observed algal blooms and hypoxia. High-frequency sensor technology, combined with 3D hydrodynamic modeling, is effective for understanding the complex flow regimes and associated water quality characteristics in ROR-type reservoirs.

Keywords: density currents; high-frequency monitoring; inflow mixing; Paldang reservoir; run-of-the-river reservoir; water quality modeling

---

1. Introduction

Human beings have created dams in running water to supply municipal, agricultural, and industrial water needs, and to produce electricity. Dams installed in rivers change the natural water environment, not only affecting the flow system, but also the transport and mixing of materials, water quality, and ecosystem [1–3]. Water quality problems caused by dam construction include, but are not limited to, prolonged discharge of turbid water to downstream areas after flood events and during flushing events [4], eutrophication and over proliferation of algae due to the accumulation of nutrients and increased residence time, and the depletion of dissolved oxygen (DO) in the lower layers under thermal stratification [5,6]. These problems are complex in time and space, due to physical, chemical, and biological interactions. Therefore, it is important to understand the transport and mixing process of contaminated river flows for water quality management of dammed reservoirs. An approach to these problems can begin with an understanding of the physical limnology mechanisms, including air-water heat exchange, thermal stratification, density inflow and mixing, outflow mixing, and wind mixing processes [1,7–10].

Among these processes, the main mechanisms affecting the transport and mixing of materials in reservoirs depend greatly on the type of reservoir and the operating conditions. For example, for a reservoir operated in the form of a run-of-the-river (ROR), where the inflow is discharged and there is little change in the water level [11], the physical and chemical properties of the influent rivers are the major determinants of the water environment in the reservoir. That is, the spatiotemporal variation of water quality is determined by how the influent flows in and how it circulates within the reservoir. This is because the inflow river acts as the main source for substances such as nutrients, suspended solids and dissolved substances that affect the water quality of the reservoir [7–10].

If the density of river water differs from that of the ambient reservoir water, a density current develops at the confluence. At this point, the density of each water body is a function of water temperature, total dissolved and suspended solids, and—in most reservoirs—differences in water temperature [7–10,12]. When the river flow enters the reservoir, the influent pushes stagnant ambient water until inertia decreases. It then flows to the upper layer, if it is less dense than the ambient water, and is called the overflow. If the river water density is higher than the surrounding water, the flow will plunge below the surface of the reservoir. After plunging, the flow propagates along the reservoir slope under the influence of gravity and is entrained at the interface with the surrounding water. This flow is called the underflow. As the flow propagates into the reservoir, it may separate from the reservoir bed and form an interflow when it encounters neutral buoyancy. For reservoir water quality management, it is important to accurately predict the density flow regime to understand the temporal and spatial distribution of dissolved and particulate nutrients and organics.

The characteristics of density flow regimes in reservoirs can be interpreted as the interaction between inertia and buoyancy [1,8–10]. Many studies have been carried out on the characteristics of density flow into lakes and reservoirs. In the field studies, the density flow characteristics were analyzed by monitoring the temperature, dye concentrations, and turbidity in time and space [13–15]. In laboratory-scale studies, inclined channel and stratification conditions were artificially created to measure the flow path of the higher-density flow, the location of the plunge and separation points, the mixing with the surrounding water bodies, and the thickness and velocity of the interflow [16–20]. In addition, studies using various numerical models have been conducted. Chung and Gu [21] used the laterally-averaged two-dimensional hydrodynamic model (CE-QUAL-W2) to analyze the behavior of high-density contaminated inflow into a stratified reservoir. Bournet et al. [22] developed a modified k-ε turbulence model with buoyancy effects to account for density characteristics in terms of separation point and entrainment in a channel with constant width and slope. Using a three-dimensional (3D) numerical model (EFDC), Hamrick and Mill [23] studied the heat transport and water temperature distribution in a reservoir, into which power generation effluents flow. Kulis and Hodges [24] conducted a study on the numerical grid resolution to capture gravity flow. Chen et al. [25] constructed a hydrodynamic model for the river-reservoir system (124.2 km) calibrated for water level, water temperature, and flow velocity, to analyze the flow regimes. Based on the calibrated model, they derived the downstream arrival time and water temperature change of the density inflows for each upstream flow condition scenario [26]. Na and Park [27] analyzed the behavior of river water flowing into a reservoir through a numerical simulation and used it to select the optimal intake location. In addition, Chung et al. [4] and An and Julien [28] analyzed the residence time of turbid water and the progression rate of interflow, by analyzing the behavior of density flow containing high turbidity in large reservoirs. Ramón et al. [29,30] surveyed the flow velocity, water temperature, electrical conductivity (EC), and turbidity at the confluence of two rivers and a reservoir, where hydraulic stratification occurs. They then applied a numerical model to analyze the mixing ratio and mixing characteristics of the two inflow sources. Vilhena et al. [31] suggested that the formation of underflow influent that includes high concentrations of nutrients, and has vertical mixing by wind, are the main sources of nutrients necessary for the primary production of phytoplankton at the reservoir surface. Chung et al. [32] also assessed the physical mixing of the influent as a major factor causing the spatial heterogeneity of *Microcystis* biomass in a stratified reservoir.

Most of the studies discussed above have theoretically analyzed the behavior of density flows under standardized experimental conditions or constructed numerical models with time–space-limited experimental data. However, these approaches are limited to generalizing the density flow and mixing characteristics of river water occurring in various reservoir types and inflow conditions. The problem becomes more difficult when the reservoir terrain is very complex, various inflow rivers interact with each other, and there are strong circulations in the reservoir water body [29,30]. Therefore, to solve these problems, a new approach combining high frequency sensor technology and 3D numerical modeling technology is needed. Sensor technology that has evolved with the 4th industrial revolution enables the introduction of an automatic high-frequency monitoring system in lakes and reservoirs. Various efforts are being made to better understand the water environment using high resolution data [33,34].

The Paldang reservoir, the subject of this study, is one of the water bodies that has such complex conditions. Three rivers with different physical and chemical properties enter the reservoir, and the dam is very close to the confluence point (Figure 1a). The retention time of the reservoir is 6 days, on average, causing the frequency of water rotation to be relatively high. Further, the impact of upstream rivers on the flow regimes and water quality of the reservoir is relatively large and rapid [35]. In addition, due to the operating characteristics of the ROR reservoir and the geographic structure resulting from rapidly increasing width and depth near the bends where the two main rivers converge, the variability in hydraulic and water quality properties is even greater [27,35,36]. Consequently, spatial distribution characteristics of water quality in Paldang reservoir are closely related to physical mixing characteristics [37–42].

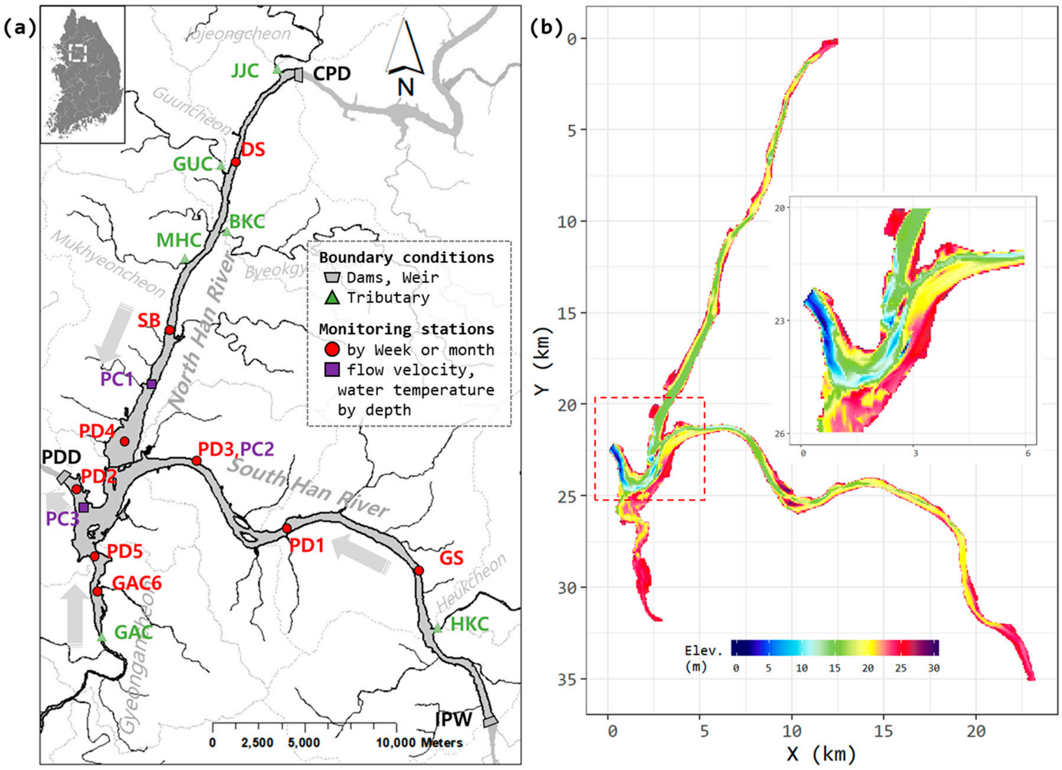

Figure 1. Boundary conditions and monitoring sites of (**a**) Paldang reservoir and its (**b**) bathymetry. Elev. means elevation above mean sea level.

The purpose of this study was to characterize the mixing and circulation of three rivers with different physicochemical properties into the Paldang reservoir, using high-frequency monitoring and 3D hydrodynamic modeling. For this purpose, high frequency in situ measurements of 3D flow and water temperature were implemented at the point of confluence and within the reservoir. A 3D hydrodynamic model was constructed and calibrated with the high-frequency data. This model was used to simulate the spatiotemporal changes of flow velocity, water temperature, residence time, and EC in the reservoir and to characterize the inflow mixing processes of the rivers. Finally, we analyzed the relationship between the physical mixing characteristics of the three rivers flowing into Paldang reservoir and the areas in which harmful algae overproliferated and hypoxia is observed.

2. Materials and Methods

2.1. Study Site

The Paldang reservoir, a component of the rivers and reservoirs system in the Han River (Republic of Korea), operates in conjunction with five dams upstream of the North Han (NH) river basin and two dams and three weirs in the South Han (SH) river basin. The NH-river, the SH-river, and Gyeongancheon stream flow into the Paldang reservoir from the north, east, and south directions, respectively (Figure 1a). The NH-river and the SH-river merge to flow southward, and then the width of the river expands and deepens. After the two rivers join, the Paldang reservoir goes through a steep curved section, joins the Gyeongancheon, heads for Paldang Dam, and then flows downstream to the West Sea. The reservoir was formed after the Paldang Dam (37°31′35.0′′ N, 127°16′44.6′′ E) was completed in 1974, establishing a system to supply power and water to the Seoul metropolitan area. The Paldang reservoir is a large-scale water source that supplies about 8 million tons of water every day to 25 million citizens near the metropolitan area. The reservoir is regulated between the normal water level of EL. 25.5 m and low water level of EL. 25.0 m. At normal water level, the total capacity is 244×10^6 m^3, the surface area is 36.5 km^2, the average depth is 6.7 m, and the maximum depth of the dam front is about 25 m. The reservoir has a complex terrain and its boundaries extend approximately 35 km to the Cheongpyeong Dam (CPD) in the direction of the NH-river, approximately 30 km to the Ipobo Weir (IPW) in the direction of the SH-river, and approximately 10 km to the confluence of the Gyeongancheon stream (GAC) in the direction of Gyeongancheon (Figure 1a). The CPD located in the NH-river intermittently discharges water only during hydropower generation, while the IPW of the SH-river is operated as a continuous discharge. The reservoir generally maintains the water level at EL. 25.0 m as it is a ROR reservoir.

2.2. Field Monitoring

The Korean Ministry of Environment operates a water quality monitoring system on a weekly or monthly basis for both the Paldang reservoir and inflowing rivers (PD1-PD5 in Figure 1a) due to the importance of the former as a source of drinking water [43]. However, due to the operation of the upstream CPD and IPW, the flow pattern in the Paldang reservoir is reported to have a diurnal variation [36]. Therefore, it is not enough to analyze the flow and water quality characteristics of the Paldang reservoir based solely on existing weekly or monthly data. Previous studies [35,38,40,41] analyzed the relationship between flow and water quality based on the hydrological parameters (i.e., water level, precipitation, inflow, discharge, and hydraulic retention time) of the entire waterbody and the weekly or monthly water quality data measurements. As a result, the sub-daily dynamic flow characteristics of the Paldang reservoir and the resulting spatial variability in water quality have been overlooked. Very few studies have been conducted using high-frequency data measurements, and those that have [36], were limited to analysis of the interactions of the three rivers, due to a lack of spaciotemporal data.

In this study, to investigate the physical mixing characteristics of the three rivers flowing into the Paldang reservoir, three sites were selected for high-frequency monitoring of water velocity and water temperature. An acoustic doppler current profiler (ADCP, Teledyne RD Instruments, Poway, CA, USA) and water temperature sensors (TR-1050 and TR-1060, RBR Ltd., Ottawa, ON, Canada) were installed at PC1 (NH-river branch) and PC2 (SH-river branch), located 10 km upstream from the Paldang Dam, and PC3 located at 1.5 km upstream from the dam (Figure 1a). Each instrument measured flow velocity and water temperature for 37 days from Julian day 133 (May 12) to 169 (June 17) in 2016, at depths of 0.2–1.0 m intervals. Flow velocity data were collected at 10-min intervals and water temperature at 10-s intervals. To maintain the vertical posture of the ADCP, it was mounted on a bottom mooring frame (trawl resistant bottom mount, TRBM) and the flow velocity was measured in an upward direction. This method is useful for measuring very small velocity changes. The NH-river branch was measured at 0.2 m depth interval, taking into account the complex mixing resulting from the intermittent discharge of the Cheongpyeong dam [36]. At the PC2 point of the SH-river branch and the PC3 point of the Paldang Dam section, the flow velocity was measured at 0.5 m depth interval. The water temperature loggers were equipped with a thermometer chain to measure at 1 m depth interval from the water surface to the bottom.

2.3. Three-Dimensional Hydrodynamic Model

2.3.1. Configuration and Application of Numerical Model

The 3D numerical model used in this study is the Aquatic Ecology Model 3D (AEM3D). This model is based on the Estuary, Lake and Coastal Ocean Model (ELCOM) and the Computational Aquatic Ecosystem Dynamics Model (CAEDYM) developed at the Centre for Water Research at the University of Western Australia [44,45]. The governing equations basically consist of a momentum equation, a continuity equation, a free surface equation, and a mass advection and diffusion equation. The hydrodynamic model solves the unsteady, viscous Navier–Stokes equations for incompressible flow, assuming the hydrostatic pressure for vertical momentum. Modeled hydrodynamic processes include barotropic and baroclinic pressures, rotational effects due to Coriolis force, wind stresses, surface thermal forcing, inflows, outflow, and transport of salts, heat, and passive scalars. The hydrodynamic algorithms are based on the Euler–Lagrange equations for advection of momentum with a conjugate-gradient solution for the free-surface height. Passive and active scalars, such as tracers, salinity, and temperature, are advected using a conservative ULTIMATE QUICKEST discretization. Detailed numerical methods for the governing equations are presented in Ref. [44,45].

The numerical grid consists of a total of 192,156 sectors, divided into 50 m × 50 m in the longitudinal (x) and transverse (y) directions and 1 m in the vertical direction (z) using the bathymetry data of the Paldang reservoir (Figure 1b). The accuracy of the numerical model grid was confirmed by comparing with the observed reservoir water level-capacity relationship, with a relative error of 3.3%. The boundary conditions of the numerical model were constructed by classifying inflow and outflow. The flows from CPD (the NH-river), IPW (the SH-river), GAC (Gyeongan Stream), and tributary streams (JJC, GUC, BKC, MHC, and HKC) were used as inflow boundary conditions (Figure 1a). Outflow boundary conditions consisted of hydroelectric power generation and gate discharge from the Paldang Dam (PDD), and intake of drinking water within the reservoir. Influent flow rate, water temperature, EC boundary conditions, and meteorological data were collected from relevant agencies [46–48]. The statistics of the data on the major boundary conditions are presented in Table 1.

EC was assumed to be conservative and simulated as passive scalar. EC is often used as an indicator of total dissolved solids (TDS) and is affected by geological characteristics of the watershed, and point and non-point source pollutants. In previous studies, the EC assessed the contribution of each tributary when two tributary streams merged [30,49] or it was used as a conservative tracer because of its relatively low contribution to reservoir water density [50].

The initial water level was set as the observation level at the start of the simulation on May 1, 2016. The initial conditions of water temperature and EC were input to the numerical grid by spatially linear interpolation, using the observed data from national measurement network points. For stabilization of the initial fields populated with the simulated values, the simulation was performed after 7 days of start-up time, considering the hydraulic residence time.

Table 1. Variations in flow rate, water temperature and electrical conductivity at main boundary conditions between Julian day 122 to 152 (May 2016) and 153 to 182 (June 2016).

Site	Flow Rate (m^3/s)		Water Temperature (°C)		Electrical Conductivity (µS/cm)	
	May	June	May	June	May	June
	(122–152)	(153–182)	(122–152)	(153–182)	(122–152)	(153–182)
CPD	157.5 ⁽¹⁾ ± 149.9 ⁽²⁾ (0 ⁽³⁾/529.9 ⁽⁴⁾)	145.1 ± 156 (0/648.2)	16 ± 0.9 (14.2/17.5)	17 ± 0.6 (16.1/18.2)	123 ± 11 (113/135)	121 ± 10 (105/128)
IPW	188.2 ± 84.5 (50.9/421.7)	73.5 ± 25.3 (0/173.5)	17.9 ± 3.9 (9.5/28.1)	21.2 ± 2.9 (14.2/28.3)	263 ± 25 (222/285)	281 ± 14 (262/292)
GAC	9.7 ± 7.1 (3.3/55.7)	4.6 ± 2 (0/19.5)	17.2 ± 4.2 (8.2/28.1)	20.7 ± 3.1 (13.2/28.3)	278 ± 43 (238/339)	421 ± 43 (365/479)
PDD	323.9 ± 176.7 (0/780)	180.1 ± 87.8 (0/543)	-	-	-	-

(1): Mean; (2): Standard deviation; (3): Min; (4): Max. CPD: Cheongpyeong Dam; IPW: Ipo Weir; GAC: Gyeongancheon; PDD: Paldang Dam.

2.3.2. Assessment of Model Performance

The hydrodynamic model of AEM3D performs water temperature simulation based on thermodynamic theory, so the default parameter values of water temperature were used [51]. The Paldang Reservoir is home to a total of nine national monitoring networks: Three sites (DS, SB, PD4) in the NH-river, three in the SH-river (GS, PD1, and PD3), two in Gyeongancheon stream (GAC6, PD5) and one near the Paldang Dam (PD2) (Figure 1a). The accuracy of the numerical model was evaluated by comparing the simulated values with the flow velocity, water temperature and EC measured at 9 National Monitoring Networks and 3 high-frequency monitoring sites (PC1-3). The mean error (ME), mean absolute error (MAE), root mean square error (RMSE), and relative error (RE) were used for evaluating the model's performance [10]. Numerical simulations were performed on a 64-bit Windows 7 box with an Intel Xeon (R) CPU operating at 3.50 GHz (32 GB memory). The simulation period was 2 months from May to June 2016, the computation time interval was 120 s, and the total computation time for the simulation period was about 18 h.

3. Results and Discussion

3.1. Flow Characteristics during Monitoring Period

The ratios of 10-year average (2007–2016) inflows into the Paldang reservoir are 54.7% from the SH-river, 42.4% from the NH-river, 2.5% from Gyeongancheon stream, and 0.4% from other sources [37]. The major inflows of the reservoir are the NH-river and the SH-river, accounting for 97.1%. In general, the inflow of the SH-river is larger than that of the NH-river. During the 2016 experiment, the ratio of flows from the three rivers into the Paldang reservoir in May was similar to the average ratio over the last decade. However, the proportion of the flow SH-river in June was only 32.8% of the total inflow, which was exceptionally low (Table 2, Figure 2). This condition was the result of the continued drought in the watershed upstream of the Paldang Dam during 2014–2016. Moreover, the flows of the NH- and SH-rivers were mainly influenced by the discharges of the dams located upstream. Under these hydrological conditions, the hydraulic retention time ($\tau = Q/V$, here, τ: hydraulic retention time, Q: total outflow, and V: volume of reservoir) of 2016 was estimated to be 8.2 days, with a range of 1.8 to 25.7 days. The residence time in May and June 2016 was estimated to be 6.6 days and 11.0 days, respectively. Compared with the 10-year averages of 7.0 and 6.5, May is similar, while June is about 1.7 times longer.

Table 2. Comparison on flow rates and the proportions of main inflows on Julian day 122 to 152 (May 2016) and 153 to 182 (June 2016).

Inflows by Branch	May 2016 (122–152)		June 2016 (153–182)	
NH-river (CPD + JJC + GUC + BKC + MHC)	167.6 m^3/s	45.3%	147.7 m^3/s	65.2%
SH-river (IPW + HKC)	193.0 m^3/s	52.1%	74.4 m^3/s	32.8%
Gyeongancheon (GAC)	9.7 m^3/s	2.6%	4.6 m^3/s	2.0%

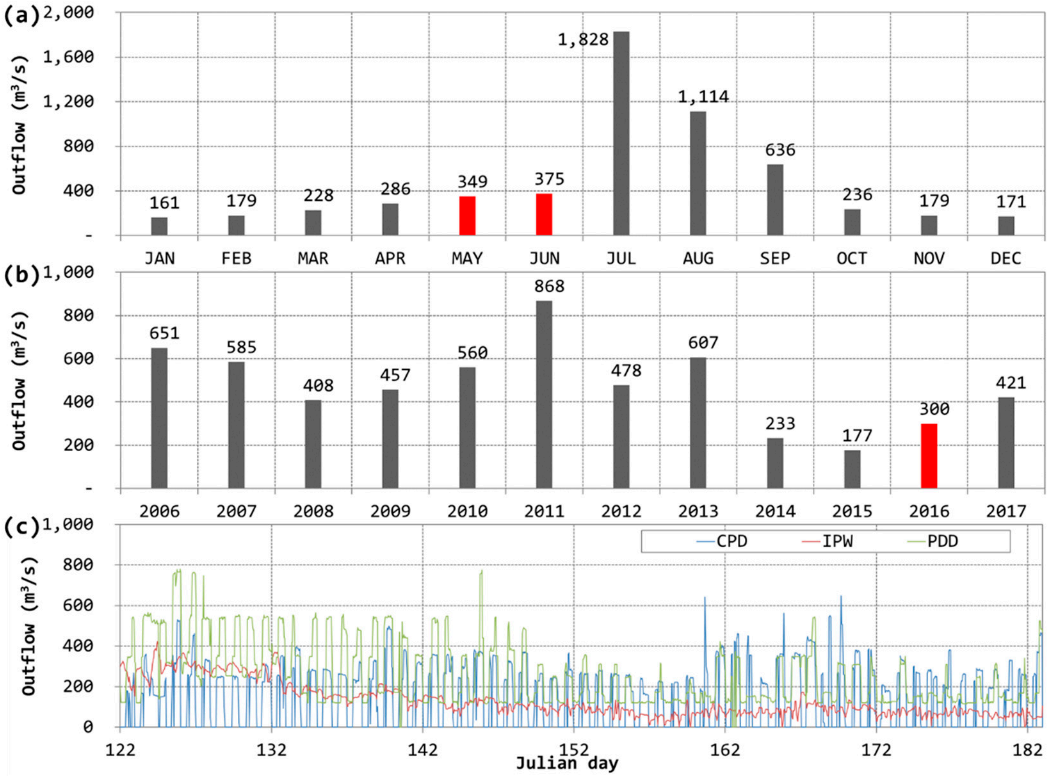

Figure 2. Discharge trend of Paldang Dam over the past 10 years. (**a**) average monthly outflow for 2006–2016; (**b**) average annual outflow for 2006–2016; and (**c**) hourly variations of discharge for Paldang Dam (PDD), Cheongpyeong Dam (CPD), and Ipo Weir (IPW) from Julian day 122 to 152 (May 2016) and 153 to 182 (June 2016).

The hourly time series of discharge at the PDD, CPD in the NH-river and IPW in the SH-river, during May and June 2016, are shown in Figure 2c. At the PDD and CPD, water is discharged only during hydropower generation, so the hydrograph is serrated, while the IPW shows continuous flow change characteristics. Since June, the discharge of the IPW rapidly decreased, due to the continued drought.

3.2. *Temporal and Spatial Variations of Flow Velocity and Water Temperature*

Figures 3 and 4 show the temporal changes of flow velocity and water temperature for each of the monitoring sites in the Paldang reservoir, measured using high-frequency sensors. At the NH-river branch (PC1), from the end of May, the upstream flow (red color in Figure 3a) occurred in the upper layer based on a depth of 2–4 m. Moreover, the downstream flow (blue color in Figure 3a) occurred in the middle and lower layers. At this time, the maximum flow velocity was observed at a 4–5 m depth. The maximum water temperatures and density gradients showed change rates of 3.7 °C/m and 0.53 $kg/m^3/m$, respectively, at a 3–4 m depth. As the water temperature stratification strengthened, the upstream flow occurred in the upper layer of the NH-river branch, and the underflow in the downstream direction predominantly occurred in the lower layer. In contrast, at the SH-river Branch (PC2), the downstream flow dominated in the upper layer, based on a depth of 5–6 m, and the upstream flow was formed in the lower layer. The maximum water temperatures and density gradients showed change rates of 2.3 °C/m and 0.40 kg/m^3/m, respectively, at a 4–5 m depth. The location of maximum water temperature and density gradient in the NH-river branch (PC1) is about 1 m higher than that of the SH-river branch (PC2). At the dam front site (PC3), downstream flow dominated the entire layer. The maximum flow velocity was found at a 5–10 m depth and the average flow velocity was less than 10 cm/s. The maximum water temperatures and density gradients showed change rates of 1.9 °C/m and 0.44 kg/m^3/m, respectively, at a 3–4 m depth.

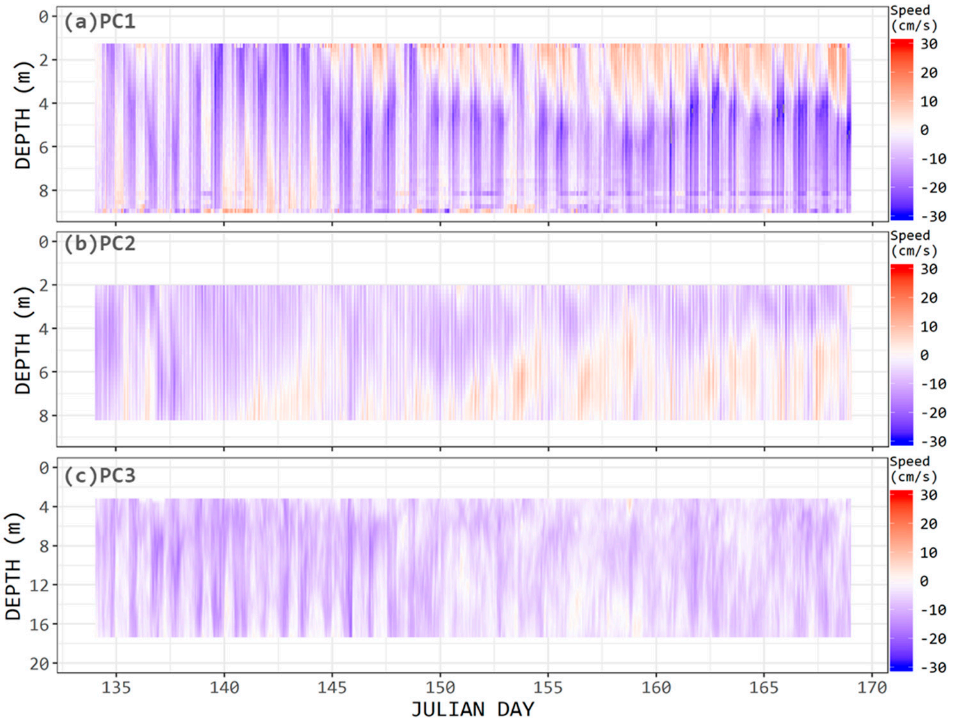

Figure 3. Observed time-depth profiles of flow velocity at (**a**) PC1, (**b**) PC2, and (**c**) PC3. The positive (+, red) and negative (–, blue) values of the color bar indicate the upstream and downstream flow, respectively. Julian day is the day of year 2016 and the depth is measured from the water surface level.

The intermittent discharge pattern of the CPD seems to have a periodic effect on the flow regime and stratification structure throughout the Paldang reservoir. The water temperature difference between the surface layer and the bottom layer showed a similar tendency to increase from about 2 °C in mid-May to 8 °C in mid-June, but the vertical distribution developed in different structures for each survey site. The PC1 and PC3 sites had a greater thickness of cold water in the lower layer than the PC2 site (Figure 4). This is because low temperature water flows into the Paldang reservoir due to the low-level discharge of the Cheongpyeong Dam in the NH-river. The mixing processes of water with a low temperature (or high density) flowing from the NH-river branch and water with a relatively high temperature (or low density) flowing from the SH-river branch are an important factor that determines the water circulation and local water environment in the Paldang reservoir. In the following section, the AEM3D model was used to simulate the high-frequency flow velocity and water temperatures measured at each station, and to interpret the mixing characteristics of two rivers with different density characteristics.

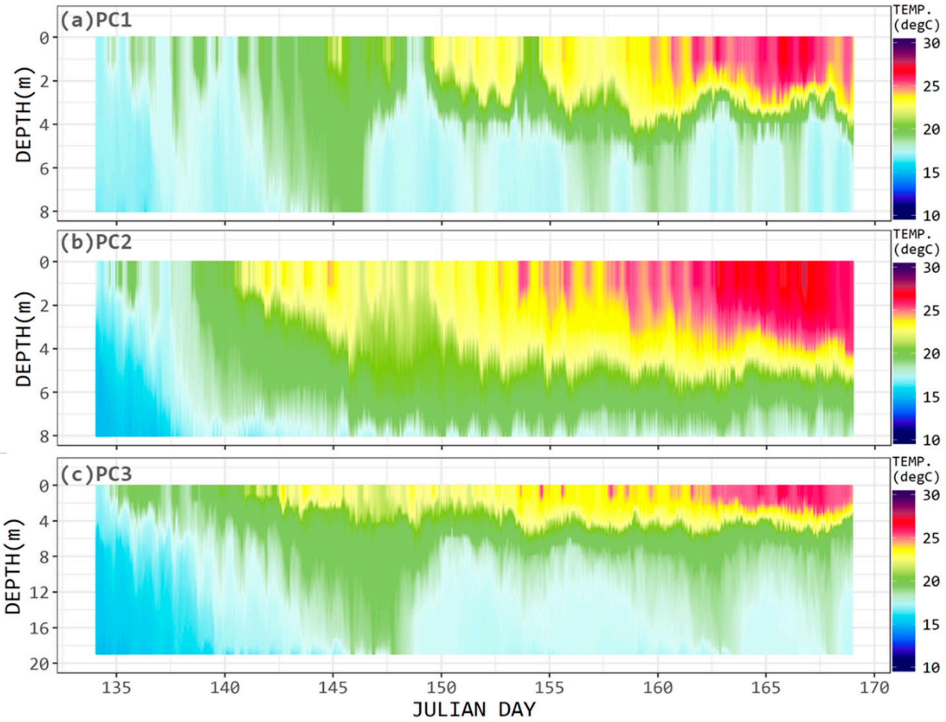

Figure 4. Observed time-depth profiles of water temperature at (**a**) PC1, (**b**) PC2, and (**c**) PC3. Julian day indicates the day of the year 2016, the temperature unit is °C, and the depth is measured from the water surface level.

3.3. Comparison of Monitoring Data and Numerical Simulation Results

The performance of the model was confirmed by comparing the water level, flow velocity, water temperature, and EC simulated by the AEM3D model with the observed data (Table 3). The error data for the water level was calculated by comparing the simulation values with the observation values in hourly units. In contrast, the errors for flow velocity and water temperature were calculated by averaging the high-frequency observations hourly and comparing these with the simulated values. In the case of EC, the observed value was measured on a weekly basis, and the errors were calculated by comparing this with the simulation value at that time. The vertical profiles of simulated and observed flow velocity, water temperature, and EC are compared and presented in Figures S1–S3. As the Paldang reservoir is a ROR-type reservoir, the water level fluctuation is low; it is maintained at EL. 25 m throughout the year. The errors between the observed and simulated water levels were estimated to be MAE 0.02 m, RMSE 0.03 m, and RE 0.1%, which were relatively small compared to previous studies [27]. The accuracy of the simulated water level confirms the reliability of the numerical grid and flow boundary conditions used in the model.

The flow velocity simulations had error ranges of ME −0.21 to 0.07 cm/s, MAE 0.95 to 1.11 cm/s, RMSE 1.22 to 1.83 cm/s, and RE 17.1% to 23.8%. The numerical model accurately simulated the bi-directional flow of the upper and lower layers of the water body in the upstream and downstream directions, respectively, at the PC1 point in the NH-river branch (Figure S1). At the PC2 point, the model accurately simulated the overall trend of the flow, but after June, the average upstream velocity in the lower layer was somewhat underestimated. This discrepancy might be due to use of the z-coordinate system in the AME3D model, which may result in numerical convective entrainment that leads to underestimation of the underflow propagation speed [52]. At the PC3 point near the Paldang Dam, the downstream flow velocity prevailed at all depths, and the simulated flow velocity distribution was reproduced accurately.

Table 3. Error statistics between observed data and Aquatic Ecosystem Model (AEM3D) simulations on water level, flow velocity, water temperature, and electrical conductivity at each site.

Stations	ME	MAE	RMSE	RE (%)
Water Level (unit: m)				
PD2	0.0 (1)	0.02	0.03	0.1
Flow Velocity (unit: cm/s)				
PC1	0.07 (1) ± 0.24 (2) (−0.67 (3)/0.75 (4))	1.11 ± 0.27 (0.54/1.97)	1.6 ± 0.5 (0.78/3.59)	17.1 ± 10.1 (4.2/55)
PC2	−0.31 ± 0.28 (−1.19/0.63)	0.95 ± 0.29 (0.29/1.8)	1.22 ± 0.38 (0.36/2.22)	23.8 ± 10.1 (4.5/51.5)
PC3	−0.21 ± 0.18 (−0.86/0.21)	1.04 ± 0.26 (0.5/1.95)	1.83 ± 0.78 (0.6/5.17)	19.8 ± 7.7 (5.1/44.3)
Water Temperature (unit: °C)				
PC1	0.2 ± 0.1 (−0.1/0.6)	0.6 ± 0.4 (0.1/1.8)	0.9 ± 0.9 (0.1/2.7)	3.3 ± 1.8 (0.6/9.3)
PC2	−0.1 ± 0.2 (−0.5/0.2)	0.4 ± 0.2 (0.1/0.8)	0.5 ± 0.2 (0.1/1.3)	1.8 ± 0.8 (0.3/4)
PC3	0.0 ± 0.03 (−0.1/0.1)	0.2 ± 0.1 (0.1/0.5)	0.3 ± 0.1 (0.1/0.8)	1.1 ± 0.4 (0.4/2.5)
Electrical Conductivity (unit: µS/cm)				
PD4	6 ± 22 (−14/53)	26 ± 17 (5/53)	35 ± 22 (6/73)	15.4 ± 10 (2.6/32.7)
PD3	−7 ± 12 (−29/3)	11 ± 12 (1/32)	17 ± 20 (2/53)	4.3 ± 4.7 (0.4/12.9)
PD2	4 ± 13 (−10/24)	22 ± 11 (8/45)	32 ± 15 (12/54)	12.2 ± 6.5 (3.8/24.7)

1 ± 2 (3/4), (1): Mean; (2): Standard deviation; (3): Min; (4): Max. Mean error (ME), mean absolute error (MAE), root mean square error (RMSE), and relative error (RE).

Prediction errors for water temperature ranged from ME −0.1 to 0.2 °C, MAE 0.2 to 0.6 °C, RMSE 0.3 to 0.9 °C, and RE 1.1% to 3.3%. The initial vertical distribution of the predicted water temperature at the PC1 point reflected the measured value distribution well, but in mid and late May, the numerical model overestimated the measured value from the surface layer to the depth of 4 m (Figure S2). Since then, the vertical distribution of water temperature was reproduced well in June, but the depth of the thermocline was somewhat lower than that of the observed data. The vertical distribution of water temperature was reproduced well at the PC2 and PC3 points, but the vertical water temperature gradient was weakly simulated, compared to actual data after mid-June.

The prediction errors for EC included an ME −7–6 µS/cm, MAE 11–26 µS/cm, RMSE 17–35 µS/cm, and RE 4.3%–15.4%, on average. The numerical model accurately simulated the overall mixing of EC in the reservoir. The EC characteristic observed at the upper layer of the PD4 site increased significantly from 126–128 µS/cm in late May to 249–285 µS/cm afterwards, while the lower layer continued to exhibit low values of 112–130 µS/cm. The simulation results from the numerical model were an accurate prediction of the changes in the vertical distribution of the EC formed by the mixture of the SH-river and the NH-river (Figure S3). At the PD3 point, the numerical model underestimated the NH-river flow intrusion to the bottom of the SH-river. As mentioned above, the error is associated with numerical convective mixing due to use of the z-coordinate system in the vertical direction [52]. The PD2 near the Paldang Dam showed a higher EC value in the upper layer than in the lower layer after May, continuing through June. The simulation results agreed with the observed pattern.

The simulated water temperature and EC of the outflow water were compared with the data measured at 4.3 km downstream of the Paldang Dam (Figure 5). The simulation results correspond to the gray lines in Figure 5, and the values obtained from the 24 h moving-average filter samples are shown in black. The prediction errors for water temperature were ME 0.1 °C, MAE 0.5 °C, RMSE 0.8 °C, and RE 2.8%. The errors for EC were ME −4 µS/cm, MAE 14 µS/cm, RMSE 18 µS/cm, and RE 7.8%. To accurately estimate the outflow water temperature and EC in the stratified reservoir, the stratification structure of the reservoir and the transport and mixing of materials from the inflow at the boundary of the Paldang dam must be properly simulated. Overall, comparison of the numerical simulations with measured data demonstrate that the AEM3D model is a good predictor of the density flow and the mixing processes of the rivers flowing into the Paldang reservoir.

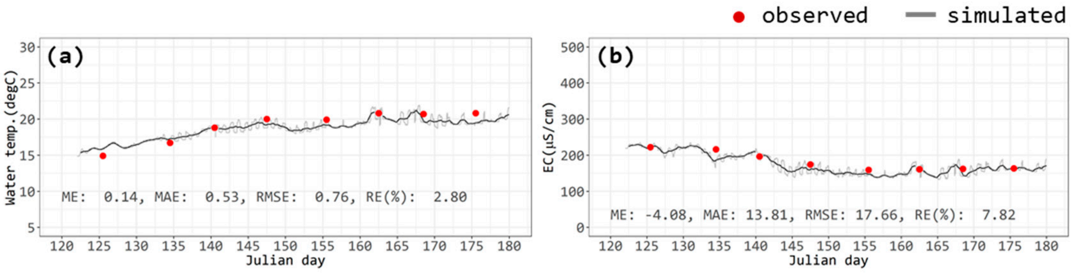

Figure 5. Comparison of temporal variations of (**a**) observed and simulated water temperature and (**b**) electrical conductivity at the outflow of Paldang Dam.

3.4. *Mixing and Circulation Characteristics of the Three Rivers in Paldang Reservoir*

3.4.1. Flow Regime and Water Stratification

Longitudinal changes of the flow speed and water temperature from the upstream boundary of each river to the Paldang Dam are presented in Figure 6 and summarized in Tables S1 and S2, divided into the NH-river branch, the SH-river branch, and the Gyeongancheon branch.

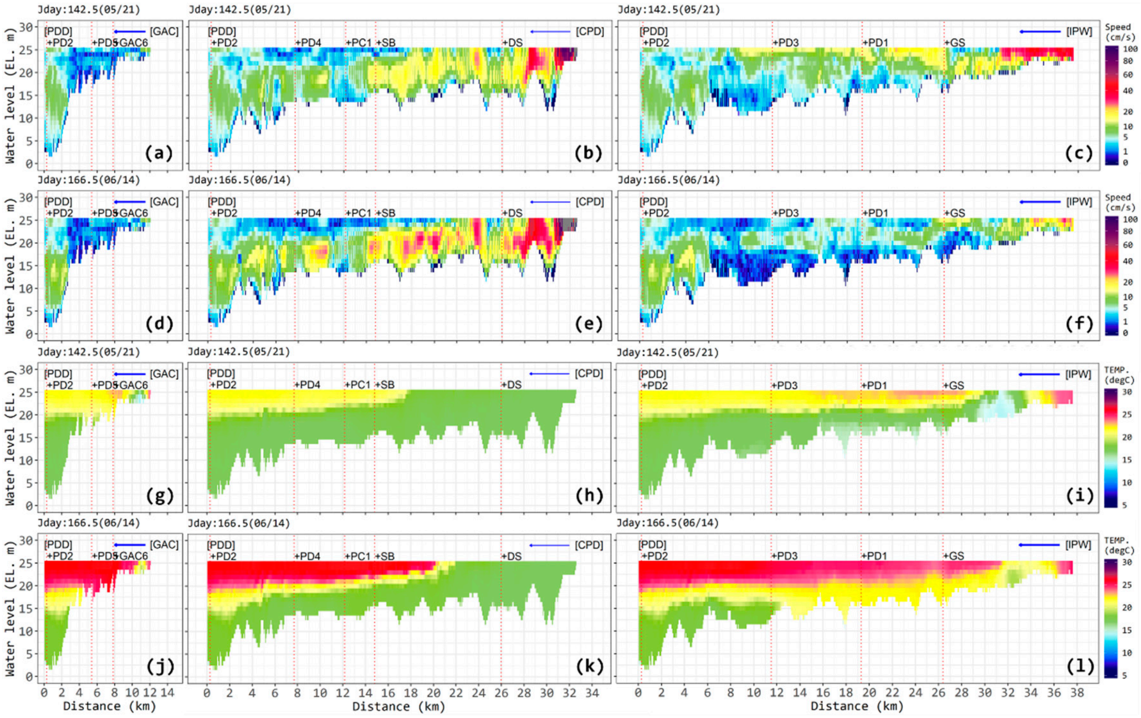

Figure 6. Longitudinal variations of (**a**–**f**) flow velocity and (**g**–**l**) water temperature on Julian day 142.5 (**a**–**c**, **g**–**i**) and 166.5 (**b**–**f**, **j**–**l**). Left snapshots from GAC to PDD; center snapshots from CPD to PDD; right snapshots from IPW to PDD. Jday and parentheses are the day of year 2016 and month/day (format: mm/dd).

The flow speed distribution of the NH-river branch (Figure 6b,e), after the plunge point appears at approximately 2–5 km upstream of the SB point, the flow velocities are high in the middle and lower layers, while the upper layer is stagnant. The NH-river influent pushes the stagnant ambient water until its inertia is arrested, whereby it becomes the underflow, due to density differences. The simulated flow speed results (Figure 6b,e) are in good agreement with the high-frequency velocity data observed at PC1 (Figure S1a), where the surface water moved toward the upstream and the middle and lower water was directed downstream. The NH-river showed a small change in inflows during May and

June (Table 1) and a small change in inflow water temperature due to lower layer discharge from the hydroelectric generation of the Cheongpyeong Dam (May 16 °C, June 17 °C). The plunge point of the NH-river influent was formed at the SB point in May, but in June, formed between the SB and DS points, as the buoyancy effect became stronger, due to the larger temperature difference between the influent and the Paldang reservoir surface water (Figure 6h,k). As this flow regime formed, the NH-river influent had a dominant effect on the lower layer flow from the NH-river branch to the dam front. At the same time, the surface layer of the NH-river branch, especially the downstream section of the plunge point, maintained a relatively high temperature and formed a stagnant zone.

The SH-river branch showed high flow speed in the upper and middle layers in May, but a lower flow speed in the lower layers (Figure 6c). However, in June, the flow rate of the SH-river decreased by 61% compared to May (Table 2), and the flow speed decreased overall (Figure 6f). In June, the average flow speed was the highest at 4 m depth at the PD1 and PD3 points, and the average flow speed at the bottom was 1.0 cm/s or less toward the upstream (Figure S1b, Figure 6c,f). Unlike the flow structure of the NH-river branch, the influent of the SH-river branch has a relatively high temperature; therefore, this influent has more influence on the upper and middle layers of the confluence section (Figure 6i,l). In the SH-river branch, the Heuckcheon stream (Figure 1a) flows between the IPW and GS points, resulting in a slight weakening of the water stratification; however, but the surface water temperature was high over the entire branch.

Gyeongancheon stream has less inflow than the NH- and SH-rivers (Table 2). Moreover, its flow is blocked by the Paldang reservoir, so the flow speed of the Gyeongancheon branch is very smaller than that of other branches (Figure 6a,d). In addition, the water temperature distribution of the corresponding section was similar to the upper water temperature of the confluence section (Figure 6g,j).

At the PD2 point in front of the Paldang Dam, the flow velocity was the greatest at 10 cm/s in the middle and bottom layers where the penstock inlet (EL. 2.35–18.02 m) was located, but the surface layer was stagnant, with an average flow velocity of less than 2 cm/s. The water temperature gradient was the largest at a depth of 4–5 m below the water surface. The water temperature in the upper layer of thermocline at the PD2 point was similar to the upper temperature in the PD3 and PD1 of the SH-river branch, and the PD5 of the Gyeongancheon branch. On the other hand, the water temperature below the thermocline tended to be similar to the low water temperature in the NH-river branch. These results can be attributed to the density flow formed by the difference in water temperature of the NH- and SH-rivers and the thermal stratification formed in the Paldang reservoir.

The results of this study agree with a previous study [36], in which intensive flow velocity measurements and water quality surveys were conducted at the confluence of the NH- and SH-rivers. At the front section of the dam, results showed a similar density flow regime in the reservoir due to the low water temperature of the NH-river influent. However, in the previous study, the application of a numerical model to the Paldang reservoir [27] showed that the extent of the effect of underflow on the SH-river branch was slightly different when the inflow of the NH-river increased. This is because the upstream boundary of the numerical model used in the previous study was set to the SB and PD1 points corresponding to the backwater influence range of the Paldang reservoir, and the flow conditions of the simulation period were different.

3.4.2. Local Retention Time (Water Age) and Water Quality Impact

The AEM3D model used in this study can calculate the water age for each cell of the numerical grid. At the start of the simulation, the water age of each grid cell (or local retention time) is assigned a zero value, and when the simulation begins, the water age increases by the rate of the model timestep. When new water enters through the reservoir upstream boundary, it is assigned a value of zero [45]. This process is repeated to estimate the water age for each cell of the whole waterbody during the simulation. While hydraulic retention time can be used as an indicator of the average residence time of a water body by dividing the volume of the water body by the discharge amount, the water age of each grid cell is an indicator that understands the water system's space–time circulation system in more detail [53,54].

The horizontal and vertical variations of water age at surface and bottom depths are presented in Figures 7 and 8, and detailed results are summarized in Tables S1 and S2. In general, the residence time of the surface layer was longer than the bottom layer in the NH-river branch, whereas the residence time of the bottom layer was longer than the surface layer in the SH-river branch. The SB and PD4 points of the NH-river branch had an average residence time of more than 10 days in June. In particular, the maximum mean residence time was simulated as 17.5 days at the surface of the SB point (Table S2). This is due to the upstream flow along the NH-river branch from the confluence section and the steady congestion of surface layer water in the downstream section of the plunge point of the NH-river.

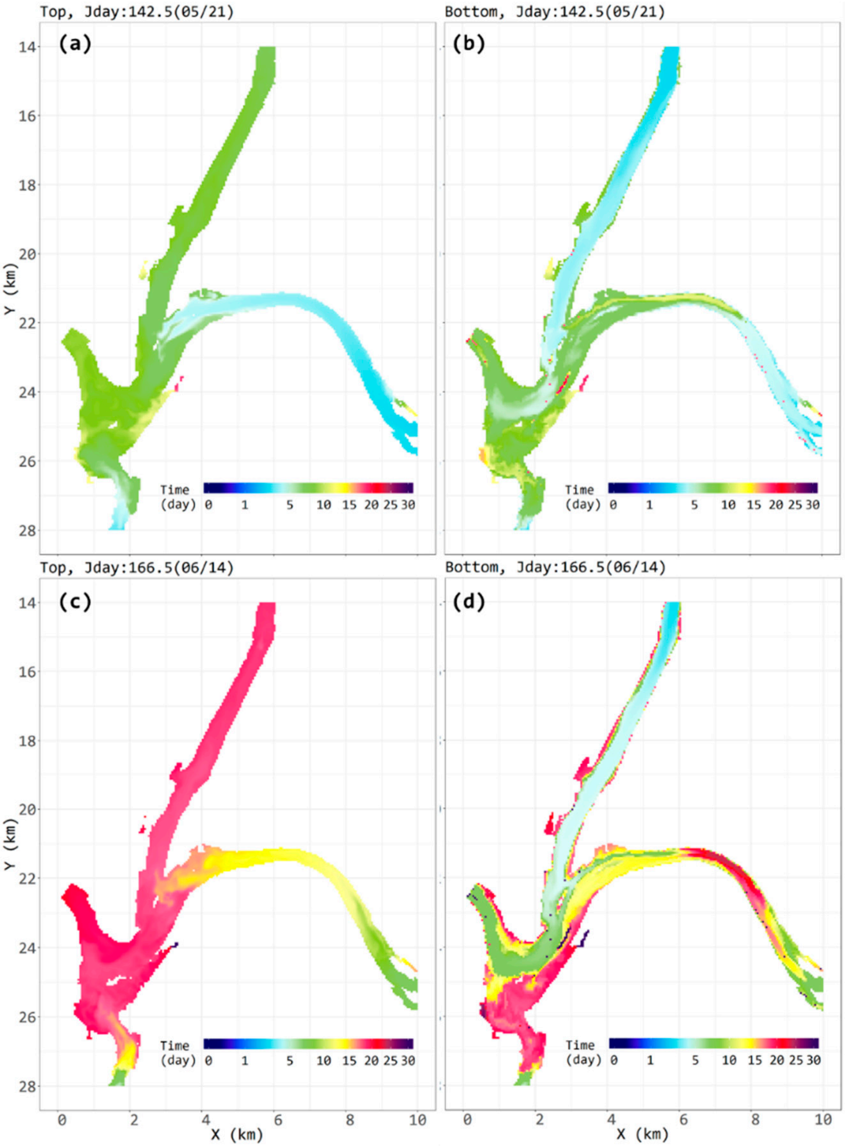

Figure 7. Horizontal variations of water age on Julian day 142.5 (**a**, **b**) and 166.5 (**c**, **d**). Left (**a**, **c**) and right (**b**, **d**) snapshots present the top and bottom layers. Jday and parentheses are the Julian day of year in 2016 and month/day (format: mm/dd).

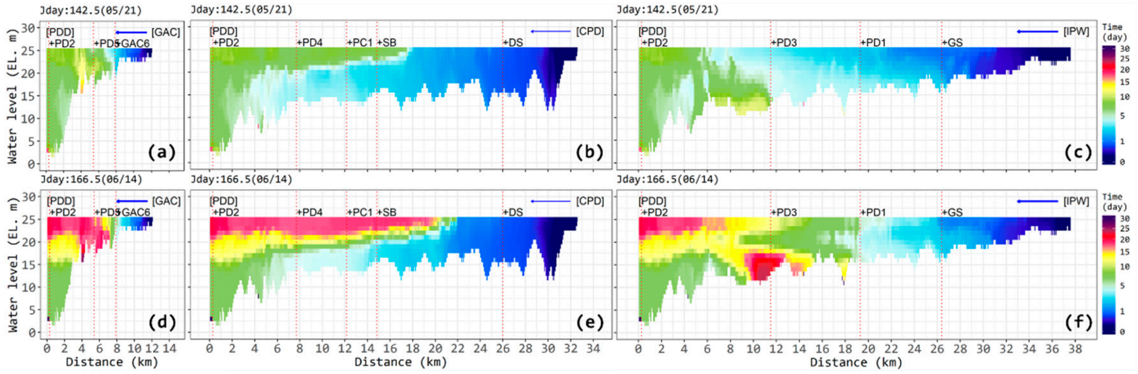

Figure 8. Longitudinal variations of water age on Julian day 142.5 (**a**–**c**) and 166.5 (**d**–**f**). Left snapshots from GAC to PDD; center snapshots from CPD to PDD; right snapshots from IPW to PDD. Jday and parentheses are the Julian day of year 2016 and month/day (format: mm/dd).

In the SH-river branch, the residence time increased continuously from the inflow boundary up to the confluence section. In June, when the inflow decreased, the residence time increased sharply to 17.9 days at the bottom layer of the PD3 point near the confluence. This is because the SH-river inflow continuously moves along the upper and middle layers until it merges with the Paldang reservoir, and the lower layer is stagnant because of underflow from the NH-river. In the Gyeongancheon branch, the residence time was more than doubled in June, compared to May. In particular, the average residence time on the surface was simulated as 14.2 days at the PD5 site in June. In the Gyeongancheon branch, the residence time was longer than that of other branches because the NH-and SH-rivers dominated the flow regime in the Paldang reservoir. At the PD2 point near the Paldang Dam, the average residence times in May and June were 5.8 and 11.2 days, respectively. In June, the residence time was 19.1 days from the surface to the depth of 2 m, but the average residence time decreased by 2.7 days at the depths of 4 to 10 m, where the average residence time was 7.5 days. Since the Paldang reservoir water is discharged downstream through the lower layer (penstock inlet EL. 2.35–18.02 m) for hydroelectricity generation, the residence time of the lower layer is shorter than the upper layer.

The area affected by algal bloom (overgrowth of harmful cyanobacteria including *Microcystis* sp., *Anabaena* sp., *Oscillatoria* sp., *Aphanizomenon* sp.), in the Paldang reservoir is closely related to the hydraulic flow characteristics formed by the influent density flows and the thermal stratification of the reservoir [38,40]. When nutrients flow from the Gyeongancheon branch and the NH- and SH-rivers, algae grows through photosynthesis in the congested waters at the confluence and are transported into the Paldang reservoir. This causes algal bloom in locally formed stagnant waters in the reservoir. Accordingly, the Korean Ministry of Environment is operating the algae alarm system (based on the number of harmful cyanobacteria cells) for the Paldang reservoir. The target areas correspond to the PD2, PD3, and SB sites that are stagnant, with long residence times shown in the simulations [41]. Comparing the density distributions of the harmful cyanobacteria measured from 2012 to 2018, it can be seen that the SB and PD2 points with longer residence times have cell densities that are about four times higher than those at the PD3 point (Figure S4).

In addition, previous studies [38–42] have reported that hypoxia occurs temporarily or long-term at the bottom of the Paldang reservoir. The hypoxia occurs due to hydraulic and hydrological conditions such as rainfall, inflow, and discharge. The spatiotemporal distribution of the NH- and SH-rivers water with different physical properties is a major determinant of the DO environment in the Paldang reservoir. The local water age simulated by the numerical model in this study can be used as a major indicator of the physical environment. As a result of classifying the points where the maximum residence time was more than 10 days in June, the upper layers of the SB and PD4 points as well as the upper and lower layers of the PD5, PD2, and PD3 points were included. The upper layers of these points have slow flow rates and high temperature environmental conditions, and the lower layers have slow flow rates and low water temperature environments. Temporal variations of DO observed by depth at sites PD2, PD3, and PD4 from 2012 to 2018 show that the lower layer at the PD2 and PD3 points, which have longer residence times, experiences hypoxia while the lower layer at the PD4 point did not (Figure S5). Although the PD3 and PD4 sites have similar water depths (about 10–12 m), the difference in residence times resulting from the density flow characteristics, led to differences in the DO environment in the lower layer.

3.4.3. Analysis of Mass Transport from Each Inflow Water Source Using Electrical Conductivity

The spatiotemporal simulation results for EC, which is assumed to be a conservative measurement parameter, were used to analyze the mass transport and mixing processes of each river entering the Paldang reservoir. The differences in the EC magnitudes in the three rivers are influenced by geological characteristics and pollutants in the upstream basin. The Gyeongancheon branch has high EC, due to the sewage treatment plant and agricultural land discharges in the basin, and the SH-river has higher EC than the NH-river, due to the wide distribution of limestone and agricultural land in the upstream basin [34,55].

The longitudinal variations in EC are presented in Figure 9, and detailed results at each site are summarized in Tables S1 and S2. The lower layer of the NH-river branch, where the NH-river influent dominates, maintained an EC value in the range of 122–130 µS/cm in May and June. When the NH-river water reached the Paldang Dam through the confluence section, EC was about 170 µS/cm in the lower part in May, but in the range of 130–140 µS/cm in June. The decrease in EC in June was due to an increase in the ratio of the NH-river inflow to the total inflow.

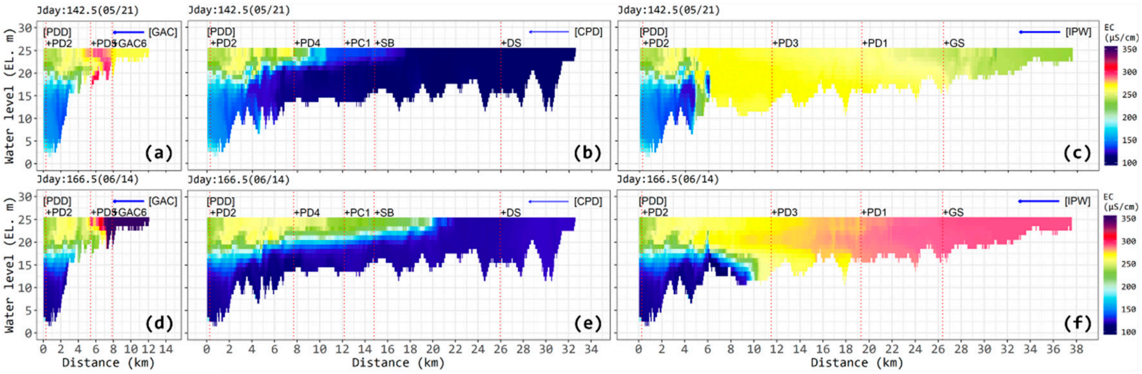

Figure 9. Longitudinal variations of electrical conductivity on Julian day 142.5 (**a**–**c**) and 166.5 (**d**–**f**). Left snapshots from GAC to PDD; center snapshots from CPD to PDD; right snapshots from IPW to PDD. Jday and parentheses are the Julian day of year 2016 and month/day (format: mm/dd).

At the PD2 point near the Paldang Dam, the EC simulation results showed that the NH-river water (lower EC) and the SH-river water (higher EC) could be found in the lower and upper reservoirs, respectively, in both May and June (Figure 9). Low EC appears in the lower layer over 6-10 km from the PDD site, due to the underflow intrusion of the NH-river (Figure 9c,f). In June, the impact nearly reached the PD3 site, due to a reduced flow rate from the SH-river (Figure 9f). In the Gyeongancheon branch, the EC at the upstream boundary increased significantly in June, compared to May, because of a reduced flow rate (Figure 9a,d). In May, the EC peaked at the PD5 point affected by the SH-river influent, but in June the EC at the PD5 point was lower than that of the upstream inflow.

The Paldang reservoir generally receives inflow at the highest flow rate from the SH-river, followed by the NH-river, and the Gyeongancheon branch, in that order. Water pollution is highest in the Gyeongancheon branch, followed by the SH-river and NH-river, in that order. Assuming the influent pollution level can be represented by the EC measure, the upper layer of the Paldang reservoir has a high concentration of pollutants, maintains high water temperature, and increases local residence time, thus providing optimal conditions for algae overgrowth. These results are in good agreement with a previous study [31] that showed that the transport and mixing processes of inflow rivers are an important mechanism for providing the nutrients necessary for the primary production of phytoplankton at the reservoir surface.

To identify the contribution of water from each river to a specific place in the Paldang reservoir, the EC values observed at the three river boundaries were treated as separate numerical tracers in the simulation. The contribution rate of EC by inflow river at the measurement point in the reservoir was calculated by dividing the EC value of each inflow source by the sum of the EC values from all rivers. Table 4 shows the results of calculating the EC contribution rate of each inflow river at each measurement point.

As a result of analyzing the EC contribution by the NH-river branch, the NH-river (CPD) contribution at the DS point was found to be about 96.8% in May. This is because the DS point is located directly downstream of the CPD. However, in the upper layer at the SB point in May, the NH-river contribution rate was 65.5% and the SH-river (IPW) contribution was 28.7%, while in June, the NH-river contribution was 9.6%, and the SH-river contribution was 80.0%. Until mid-May, the influence of the NH-river remained high, but afterwards, the difference in water temperature of the influent increased and the water temperature stratification strengthened, due to the significant increase of the SH-river inflow to the upper layer. At the PD4 point, the phenomenon seen at the SB point is seen even more clearly. From the surface to the lower layer, contributions from the NH-river increased while those from the SH-river decreased. In June, EC values at the surface layer (0.5 m from the water surface) indicated inflow contributions of 83.4% from the SH-river and 3.9% from the NH-river. At the lower layer (8.0 m from the water surface), the NH-river contribution was 87.9% and the SH-river was 8.3%. The contribution of the SH-river inflow was largest at the surface layer. The influence of the SH-river influent reached the DS point in the NH-river branch.

In the SH-river branch (IPW), the EC contribution in May remained above 98% at all depths, with no contribution seen from the NH-river. However, in June, the NH-river contributed 4.8% at the lower layer (8.0 m from the water surface) of the PD3 point, and other rivers contributed 1.8%. Comparing the high-frequency flow velocity data (Figure S1b) and the EC measurement values, the results of the numerical simulations seem to underestimate the influence of the NH-river influent on the SH-river, possibly due to the numerical convective mixing between underflow and overlying water [52]. The NH-river inflow in June was expected to have a greater impact on the lower layer of the SH-river branch than the simulation results showed.

Regarding evaluation of the Gyeongancheon branch contributions, the GAC6 point adjacent to the inflow boundary of the reservoir shows that more than 99% of the inflow originates from the Gyeongancheon branch. The PD5 point located in a shallow and wide area is most affected by the Gyeongancheon inflow. In addition, the inflow from the Gyeongancheon branch is blocked by the confluence of the NH-and SH-rivers, so that it mainly moves along the surface [27]. At the PD2 point in front of the Paldang Dam, the contributions of the NH-river increased and those from the SH-river decreased, from the surface to the lower layers. From May to June, the contribution of the SH-river decreased in the middle and lower layers.

As the NH- and SH-rivers and the Gyeongancheon branch inflows were introduced to the reservoir, the distribution of EC in the Paldang reservoir indicated complex spaciotemporal mixing characteristics. The NH- and SH-rivers accounted for most of the inflows, indicating that the mixing of the two rivers dominated the flow of material in the Paldang reservoir. The difference in density, formed by the difference in water temperature of the influent rivers, reinforces the water temperature stratification of the NH-river branch. The SH-river inflow not only counterflows to the DS point of the NH-river branch, but also affects the transport and diffusion of pollutants. Also, during the simulation, the NH-river water, with relatively high density, dominated the lower layer of the Paldang reservoir. This prevented the inflow of the SH-river into the lower layer of the Paldang reservoir and caused congestion in the lower SH-river branch.

Table 4. Contributions of each inflow boundary condition at each monitoring point (unit: %).

Boundary Conditions		**NH-River**					**SH-River**							**Gyeongan-Cheon**	**Paldang Dam**				**Paldang Dam Outflow**
		DS	**SB**	**PD4**			**GS**	**PD1**			**PD3**			**GAC6**	**PD5**	**PD2**			
		(0.5) [1]	**(0.5)**	**(0.5)**	**(4.0)**	**(8.0)**	**(0.5)**	**(0.5)**	**(4.0)**	**(8.0)**	**(0.5)**	**(4.0)**	**(8.0)**	**(0.5)**	**(0.5)**	**(0.5)**	**(10.5)**	**(20.0)**	
May (122-152) [2]	CPD	96.8	65.5	24.8	67.1	92.9	-	-	-	-	-	-	-	-	3.8	8.5	49.2	56.0	36.3
	IPW	-	28.7	70.0	26.9	0.3	98.1	98.4	98.2	98.1	98.5	98.4	98.4	0.1	19.1	78.8	46.2	38.6	57.7
	GAC	-	0.4	1.8	0.2	-	-	-	-	-	-	-	-	99.8	76.5	10.8	0.1	-	2.4
	Others	3.2	5.4	3.4	5.9	6.8	1.9	1.6	1.8	1.9	1.5	1.6	1.6	0.0	0.6	1.8	4.3	5.3	3.6
June (153-182) [3]	CPD	97.7	9.6	3.9	18.7	87.9	-	-	-	-	-	-	4.8	0.1	3.5	6.8	60.6	81.7	56.3
	IPW	0.4	80.0	83.4	72.2	8.3	99.0	99.0	99.1	98.8	98.7	98.9	93.3	0.5	28.7	75.0	34.8	14.0	38.4
	GAC	-	8.5	11.2	7.2	0.9	-	-	-	-	0.1	-	-	99.4	67.2	16.5	1.9	1.2	2.7
	Others	1.9	1.8	1.4	2.1	2.8	1.0	1.0	0.9	1.2	1.2	1.1	1.8	0.0	0.6	1.6	2.7	3.1	2.6

[1]: The numbers in parentheses are depths from water surface (unit: m); [2]: Julian day 122 to 152 (May 2016); [3]: Julian day 153 to 182 (June 2016).

In previous studies [36,56], from April to September the NH-river inflow maintained lower water temperatures than the SH-river inflow, and it is reported that the inflows of the two rivers form the hydraulic force in the Paldang reservoir. In addition, this hydraulic force affects the transport and diffusion of organic matter and nutrients and reaches the front of the dam. At the same time, the authors speculate that the relatively nutrient-rich inflow of the SH river reaches the photic layer near the Paldang dam, which may affect algal growth. Previous study conclusions are more clearly supported by the assessment of inflow-river contributions based on EC simulations.

4. Conclusions

In this study, the density flow regimes, and mixing processes of three contributing rivers, which enter the ROR Paldang reservoir with different physical and chemical properties, were intensively analyzed using high-frequency monitoring and 3D hydrodynamic simulations. The AEM3D model reproduced well the spatiotemporal variations of flow velocity, water temperature, and EC observed in the reservoir, with acceptable error rates, and was used to analyze the mixing and circulation characteristics of the river flows into the reservoir.

The spatiotemporal arrangement of the inflows and their mixing in the reservoir are largely controlled by the buoyancy force resulting from the water temperature difference in the NH- and SH-rivers. Low temperature water flows into the NH-river branch in the Paldang reservoir due to cold water discharge from the upstream dam (CPD) located on the NH-river for hydropower generation. In the Paldang reservoir, the water-temperature stratification is strengthened by the warmer overflow from the SH-river and atmospheric temperature rise. The relatively cold NH-river influent settles as it enters the Paldang reservoir, forming an underflow and proceeding to the dam along the middle and lower layers. The SH-river influent forms a surface buoyant overflow with the inertia force dissipating and the buoyancy force dominating. The SH-river overflow then proceeds upstream of the NH-river branch, due to the difference in density from the NH-river underflow. At the same time, the NH-river underflow collects in the lower layer of the SH-river branch to form a stagnant water body. The Gyeongancheon branch influent has a relatively small flow rate with high water temperature and affects the upper layer of the reservoir. Near the Paldang Dam, the NH-river inflow with low water temperature prevails in the lower layer and the SH-river and Gyeongancheon inflows with high water temperature are dominant in the upper layer.

The mixing and circulation characteristics of the NH- and SH-rivers driven by density currents were found to be the major determinants of spatial heterogeneity of water quality in the Paldang reservoir. The stagnant areas with long residence times corresponded well with spaces where harmful algal blooms and hypoxia have occurred. The upper layer in the stagnant areas has higher water temperatures, long residence time, and nutrient-rich waters from the SH-river and the Gyeongancheon branch, thus providing optimal conditions for algae proliferation. In particular, the warmer SH-river overflow propagates upstream along the NH-river, forming a stagnant area near the plunge point of the NH-river, which coincides with the area where harmful cyanobacteria blooms often occur. In addition, the difference in residence time formed in the lower layers of the NH- and SH- river branches lead to differences in the DO environment, although they have similar water depth.

This study demonstrates that 3D hydrodynamic modeling, combined with high-frequency sensor technology, is an effective tool to understand the complex flow regimes and associated water quality characteristics in ROR-type reservoirs. Further research of the hydrodynamic model constructed in this study should include water quality and ecological models. In addition, if high-frequency water quality data are collected in real-time and fed into the 3D numerical model, reservoir managers can respond quickly to water quality problems and reservoir water management can be more scientific and smarter.

Supplementary Materials: The following are available online at http://www.mdpi.com/2073-4441/12/3/717/s1, Figure S1: Comparison of observed and simulated value of vertical flow velocity at PC1, PC2, and PC3; Figure S2: Comparison of observed and simulated value of vertical water temperature at PC1, PC2, and PC3; Figure S3: Comparison of observed and simulated value of vertical electrical conductivity at PD4, PD3, and PD2; Figure S4: Box plots showing the cell density of harmful algae observed at site PD2, PD3, and SB from 2012 to 2018; Figure S5: Temporal variations of dissolved oxygen observed by depths at site PD2, PD3, and PD4 from 2012 to 2018; Table S1: Variations of averaged flow velocity, water temperature, water age and electrical conductivity with depths at the station (PD4) in May and June, 2016; Table S2: Variations of averaged flow velocity, water temperature, water age and electrical conductivity with depths at the stations in May and June, 2016.

Author Contributions: Conceptualization, I.R. and S.C.; Methodology, I.R.; Validation, I.R.; Formal Analysis, I.R.; Investigation, I.R.; Data Curation, I.R. and S.C.; Writing—Original Draft Preparation, I.R.; Writing—Review & Editing, S.C.; Visualization, I.R.; Supervision, S.C.; Project Administration, S.Y.; Funding Acquisition, S.Y. All authors have read and agreed to the published version of the manuscript.

Funding: This research was supported by Han River Environment Research Center, National Institute of Environment Research (NIER).

Acknowledgments: The authors would like to express their gratitude to Korea Agency for National Institute of Environment Research (NIER) for their valuable data and funds. The authors would like to thank the reviewers for their detailed comments and suggestions for the manuscript.

Conflicts of Interest: The authors declare no conflict of interest.

References

1. Ford, D.E.; Johnson, M.C. *An Assessment of Reservoir Density Currents and Inflow Processes*; technical report E-83-7; United States Army Engineer Waterways Experiment Station: Vicksburg, MS, USA, 1983.
2. Pisaturo, G.R.; Righetti, M.; Dumbser, M.; Noack, M.; Schneider, M.; Cavedon, V. The role of 3D-hydraulics in habitat modelling of hydropeaking events. *Sci. Total Environ.* **2017**, *575*, 219–230. [CrossRef] [PubMed]
3. Pisaturo, G.R.; Righetti, M.; Castellana, C.; Larcher, M.; Menapace, A.; Premstaller, G. A procedure for human safety assessment during hydropeaking events. *Sci. Total Environ.* **2019**, *661*, 294–305. [CrossRef] [PubMed]
4. Chung, S.W.; Hipsey, M.R.; Imberger, J. Modelling the propagation of turbid density inflows into a stratified lake: Daecheong Reservoir, Korea. *Environ. Model. Softw.* **2009**, *24*, 1467–1482. [CrossRef]
5. Imberger, J.; Marti, C.L.; Dallimore, C.; Hamilton, D.P.; Escriba, J.; Valerio, G. Real-time, adaptive, self-learning management of lakes. In Proceedings of the 37th IAHR World Congress, Kuala Lumpur, Malaysia, 13–18 August 2017.
6. Scavia, D.; Allan, J.D.; Arend, K.K.; Bartell, S.; Beletsky, D.; Bosch, N.S.; Brandt, S.B.; Briland, R.D.; Daloğglu, I.; DePinto, J.V.; et al. Assessing and addressing the re-eutrophication of Lake Erie: Central basin hypoxia. *J. Great Lakes Res.* **2014**, *40*, 226–246. [CrossRef]
7. Fischer, H.B.; List, E.J.; Koh, R.C.; Imberger, J.; Brooks, N.H. *Mixing in Inland and Coastal Waters*; Academic Press: New York, NY, USA, 1979; pp. 150–228.
8. Imberger, J.; Patterson, J.C. *Advances in Applied Mechanics: Physical Limnology*; Academic Press: Boston, MA, USA, 1990; Volume 27, pp. 303–475.
9. Martin, J.L.; McCutcheon, S.C. *Hydrodynamics and Transport for Water Quality Modeling*; CRC Press, Inc.: New York, NY, USA, 1999; pp. 335–384.
10. Ji, Z.G. *Hydrodynamics and Water Quality: Modeling Rivers, Lakes, and Estuaries*; John Wiley & Sons, Inc.: New Jersey, NY, USA, 2008; pp. 509–566.
11. McManamay, R.A.; Oigbokie, C.O.; Kao, S.C.; Bevelhimer, M.S. Classification of US hydropower dams by their modes of operation. *River Res. Appl.* **2016**, *32*, 1450–1468. [CrossRef]
12. Gill, A.E. *Atmosphere-Ocean Dynamics*; Academic: New York, NY, USA, 1982; pp. 599–600.
13. Serruya, S. The mixing patterns of the Jordan River in Lake Kinneret. *Limnol. Oceanogr.* **1974**, *19*, 175–181. [CrossRef]
14. Carmack, E.C.; Gray, C.B.; Pharo, C.H.; Daley, R.J. Importance of lake-river interaction on seasonal patterns in the general circulation of Kamloops Lake, British columbia. *Limnol. Oceanogr.* **1979**, *24*, 634–644. [CrossRef]
15. Fischer, H.B.; Smith, R.D. Observations of transport to surface waters from a plunging inflow to Lake Mead. *Limnol. Oceanogr.* **1983**, *28*, 253–272. [CrossRef]
16. Akiyama, J.; Stefan, H.G. Plunging flow into a reservoir: Theory. *J. Hydraul. Eng. Asce* **1984**, *110*, 484–499. [CrossRef]

17. Hauenstein, W.; Dracos, T. Investigation of plunging density currents generated by inflows in lakes. *J. Hydraul. Res.* **1984**, *22*, 157–179. [CrossRef]
18. Wells, M.G.; Wettlaufer, J.S. The long-term circulation driven by density currents in a two-layer stratified basin. *J. Fluid Mech.* **2007**, *572*, 37–58. [CrossRef]
19. Wells, M.G.; Nadarajah, P. The intrusion depth of density currents flowing into stratified water bodies. *J. Phys. Oceanogr.* **2009**, *39*, 1935–1947. [CrossRef]
20. Cortés, A.; Rueda, F.; Wells, M. Experimental observations of the splitting of a gravity current at a density step in a stratified water body. *J. Geophys. Res. Ocean.* **2014**, *119*, 1038–1053. [CrossRef]
21. Chung, S.; Gu, R. Two-dimensional simulations of contaminant currents in stratified reservoir. *J. Hydraul. Eng.* **1998**, *124*, 704–711. [CrossRef]
22. Bournet, P.; Dartus, D.; Tassin, B.; Vincon-Leite, B. Numerical investigation of plunging density current. *J. Hydraul. Eng.* **1999**, *125*, 584–594. [CrossRef]
23. Hamrick, J.M.; Mills, W.B. Analysis of water temperatures in Conowingo pond as influenced by the Peach Bottom Atomic Power Plant thermal discharge. *Environ. Sci. Policy* **2000**, *3*, 197–209. [CrossRef]
24. Kulis, P.; Hodges, B.R. Modeling gravity currents in shallow bays using a sigma coordinate model. In Proceedings of the 7th International Conference on Hydroscience and Enginnering, Philadelphia, PA, USA, 10–13 September 2006.
25. Chen, G.; Fang, X.; Devkota, J. Understanding flow dynamics and density currents in a River-Reservoir System under upstream reservoir releases. *Hydrol. Sci. J.* **2016**, *61*, 2411–2426. [CrossRef]
26. Chen, G.; Fang, X. Sensitivity analysis of flow and temperature distributions of density currents in a River-Reservoir System under upstream releases with different durations. *Water* **2015**, *7*, 6244–6268. [CrossRef]
27. Na, E.H.; Park, S.S. A hydrodynamic modeling study to determine the optimum water intake location in Lake Paldang, Korea. *J. Am. Water Resour. Assoc.* **2005**, *41*, 1315–1332. [CrossRef]
28. An, S.; Julien, P.Y. Three-dimensional modeling of turbid density currents in Imha Reservoir, South Korea. *J. Hydraul. Eng.* **2014**, *140*, 5. [CrossRef]
29. Ramón, C.L.; Hoyer, A.B.; Armengol, J.; Dolz, J.; Rueda, F.J. Mixing and circulation at the confluence of two rivers entering a meandering reservoir. *Water Resour. Res.* **2013**, *49*, 1429–1445. [CrossRef]
30. Ramón, C.L.; Armengol, J.; Dolz, J.; Prats, J.; Rueda, F.J. Mixing dynamics at the confluence of two large rivers undergoing weak density variations. *J. Geophys. Res. Ocean.* **2014**, *119*, 2386–2402. [CrossRef]
31. Vilhena, L.C.; Hillmer, I.; Imberger, J. The role of climate change in the occurrence of algal blooms: Lake Burragorang, Australia. *Limnol. Oceanogr.* **2010**, *55*, 1188–1200. [CrossRef]
32. Chung, S.W.; Imberger, J.; Hipsey, M.R.; Lee, H.S. The influence of physical and physiological processes on the spatial heterogeneity of a *Microcystis* bloom in a stratified reservoir. *Ecol. Model.* **2014**, *289*, 133–149. [CrossRef]
33. Cremona, F.; Laas, A.; Nõges, P.; Nõges, T. High-frequency data within a modeling framework: On the benefit of assessing uncertainties of lake metabolism. *Ecol. Model.* **2014**, *294*, 27–35. [CrossRef]
34. Marce, R.; George, G.; Buscarinu, P.; Deidda, M.; Dunalska, J.; Eyto, E.; Flaim, G.; Grossart, H.P.; Istvanovics, V.; Lenhardt, M.; et al. Automatic high frequency monitoring for improved lake and reservoir management\. *Environ. Sci. Technol.* **2016**, *50*, 10780–10794. [CrossRef]
35. Kong, D.S. Phosphorus budget of a river reservoir, Paldang. *J. Korean Soc. Water Environ.* **2018**, *34*, 270–284.
36. National Institute of Environmental Research. *Multidimensional Analysis on Material Transport in Lake Paldang (II)*; National Institute of Environmental Research: Incheon, Korea, 2008; pp. 37–77.
37. National Institute of Environmental Research. *A Comprehensive Study on Water Quality Control of Paldang Watershed (II): Hydrodynamics Characteristics*; National Institute of Environmental Research: Incheon, Korea, 2016; pp. 1–2.
38. Shin, J.K.; Hwang, S.J.; Kang, C.K.; Kim, H.S. Limnological charateristics of the river-type Paltang Reservoir, Korea. *Korean J. Limnol.* **2003**, *36*, 242–256.
39. National Institute of Environmental Research. *A Comprehensive Study on Water Quality Control of Paldang Watershed (III): Establish of Water Quality Evaluation System*; National Institute of Environmental Research: Incheon, Korea, 2017; pp. 10–12.
40. Hwang, S.J.; Kim, K.H.; Park, C.H.; Seo, W.B.; Choi, B.G.; Eum, H.S.; Park, M.H.; Noh, H.R.; Sim, Y.B.; Shin, J.K. Hydro-meteorological effects on water quality variability in Paldang reservoir, confluent area of

the South-Han River-North-Han River-Gyeongan Stream, Korea. *Korean J. Ecol. Environ.* **2016**, *49*, 354–374. [CrossRef]

41. Ministry of Environment. *Occurrence of Algae and Corresponding Annual Report (2017)*; Ministry of Environment: Sejong, Korea, 2018; pp. 2–20.
42. Park, H.K.; Byeon, M.S.; Choi, M.J.; Kim, Y.J. The effect factors on the growth of phytoplankton and the sources of organic matters in downstream of South-Han River. *J. Korean Soc. Water Environ.* **2008**, *24*, 556–642.
43. Ministry of Environment. *Operation Plan for National Water Quality Monitoring System (2017)*; Ministry of Environment: Sejong, Korea, 2017; pp. 59–164.
44. Hodges, B.R. *Numerical Techniques in CWR-ELCOM (Code Release v.1)*; University of Western Australia Technical Publication: Perth, Australia, 2000; pp. 1–35.
45. Hodges, B.R.; Dallimore, C. *Aquatic Ecosystem Model: AEM3D v1.0 User Manual*; Hydronumerics: Melbourne, Australia, 2016; pp. 1–103.
46. Water Resources Management Information System. Available online: http://www.wamis.go.kr (accessed on 1 April 2018).
47. Korea Meteorological Administration. Available online: http://data.kma.go.kr (accessed on 1 April 2018).
48. Water Environment Information System. Available online: http://water.nier.go.kr (accessed on 1 April 2018).
49. Moore, R.D.; Richards, G.; Story, A. Electrical conductivity as an indicator of water chemistry and hydrologic process. *Streamline Watershed Manag. Bull.* **2008**, *8*, 11–15.
50. Cortés, A.; Fleenor, W.E.; Wells, M.G.; de Vicente, I.; Rueda, F.J. Pathways of river water to the surface layers of stratified reservoirs. *Limnol. Oceanogr.* **2014**, *59*, 233–250. [CrossRef]
51. Lee, H.S.; Chung, S.W.; Ryu, I.G.; Choi, J.K. Three-dimensional modeling of thermal stratification of a deep and dendritic reservoir using ELCOM model. *J. Hydro Environ. Res.* **2013**, *7*, 124–133. [CrossRef]
52. Dallimore, C.; Hodges, B.R.; Imberger, J. Coupling an underflow model to a three-dimensional hydrodynamic model. *J. Hydraul. Eng.* **2003**, *129*, 748–757. [CrossRef]
53. Li, Y.; Achary, K.; Yu, Z. Modeling impacts of Yangtze River water transfer on water ages in Lake Taihu, China. *Ecol. Eng.* **2011**, *37*, 325–334. [CrossRef]
54. Delhez, E.J.M.; Campin, J.M.; Hirst, A.C.; Deleersnijder, E. Toward a general theory of the age in ocean modelling. *Ocean Model.* **1999**, *1*, 17–27. [CrossRef]
55. Ryu, J.S.; Chang, H.W.; Lee, K.S. Hydrogeochemistry and isotope geochemistry of the Han River system: A summary. *J. Geo. Soc. Korea* **2008**, *44*, 467–477.
56. Kim, J.M.; Park, J.D.; Noh, H.R.; Han, M.S. Changes of seasonal and vertical water quality in Soyang and Paldang River-reservoir System, Korea. *Korean J. Limonl.* **2002**, *35*, 10–20.